Int J Fract (2022) 238:165–183
https://doi.org/10.1007/s10704-022-00658-8

ORIGINAL PAPER

The effect of constituent particles on the tear resistance of three 6000-series aluminium alloys

Kristin Qvale · **Susanne Thomesen** · **Odd Sture Hopperstad** · **Tore Børvik**

Received: 3 March 2022 / Accepted: 8 July 2022 / Published online: 12 August 2022

Abstract This paper investigates the tear resistance of three cast and homogenized 6000-series alloys, namely AA6061, AA6063 and AA6110, all in temper T6, by means of Kahn tear tests. Of each alloy one commercial version and one tailor-made version were studied. The tailor-made alloys were designed to have approximately three times higher content of constituent particles by increasing the amount of Fe and Si in the chemical composition. The aim was to study in what way a higher constituent-particle content affects the tear resistance and properties of the alloys. The research showed that the unit initiation and propagation energies measured from the Kahn tear tests are markedly reduced when the constituent-particle content is increased, and that the tear resistance is reduced by a higher fraction than the failure strain of the smooth tensile tests. No major differences in the fracture mode and the fracture mechanisms between the alloys with normal and with high constituent-particle content were revealed by the use of computed tomography scanning or scanning electron microscopy imaging. It was concluded for the alloys studied that the increased content of constituent particles had a significant effect on the tear resistance, while the fracture mode and mechanisms remained the same.

Keywords Al–Mg–Si alloys · Kahn tear tests · Mode I · Slant fracture · Computed tomography (CT) · Scanning electron microscopy (SEM)

1 Introduction

Aluminium alloys contain particles of various sizes. As ductile fracture is governed by nucleation, growth and coalescence of voids, these particles and their interplay with the matrix become important for the fracture mechanisms. The toughness of an alloy defines its resistance to crack extension, and it follows that the ductile fracture mechanisms (and what affects these) are essential components for the toughness. For ideal toughness, a combination of high ductility and high strength is desired, but strength often comes at the cost of ductility, and normally higher yield strengths involve a net reduction in toughness (Hahn and Rosenfield 1975; Dumont et al. 2003; Petit et al. 2019).

The three particle groups that affect fracture in aluminium alloys are coarse constituent particles, dispersoids and precipitates. There is agreement that the coarse constituent particles have the strongest influence on toughness and ductility (Blind and Martin 1983; Liu et al. 2004). The constituent particles may crack at low strains, and thus initiate the fracture process

K. Qvale (✉) · S. Thomesen · O. S. Hopperstad · T. Børvik
Structural Impact Laboratory (SIMLab), Department of Structural Engineering, NTNU – Norwegian University of Science and Technology, 7491 Trondheim, Norway
e-mail: kristin.qvale@ntnu.no

S. Thomesen · O. S. Hopperstad · T. Børvik
Centre for Advanced Structural Analysis (CASA), NTNU – Norwegian University of Science and Technology, 7491 Trondheim, Norway

(Broek 1973; Hahn and Rosenfield 1975). The ligaments between the voids nucleated at the constituent particles may then fail by void sheeting involving voids nucleated at dispersoids or precipitates (Broek 1973; Hahn and Rosenfield 1975; Sutton et al. 1997; Bron et al. 2004).

The effect of the constituent particles on the ductility is purely detrimental, and they otherwise serve no useful purpose in structural alloys (Polmear 2006). By multiscale modelling, Liu et al. (2004) found that the intrinsic ductility of two Al–Cu–Mg and Al–Mg–Si alloys is halved by the presence of 1% constituent particles. In numerical simulations with discretely modelled particles in a porous plasticity matrix, Srivastava et al. (2014) found that for the lower inclusion contents the fracture toughness decreased rapidly with increasing inclusion content, while for the higher inclusion contents there was no decrease in toughness with increasing inclusion content. Tomstad et al. (2021) studied the influence of the volume fraction of constituent particles on the tensile ductility of cast and homogenized and extruded 6000-series aluminium alloys. They found that the negative effect of increased constituent particle content on the tensile ductility is significant in the cast and homogenized condition, but markedly reduced in the extruded condition. Bron et al. (2004) performed a range of mechanical tests on one commercial variant and one high-purity variant of a 2024 aluminium alloy, with a notable improvement on the damage resistance by the reduced particle content in the high-purity variant. The dispersoids may contribute to distribute slip, which may increase the toughness (Blind and Martin 1983). They may also decrease the detrimental effect of the precipitates on ductility (Liu et al. 2004). The precipitates' detrimental effect on ductility is closely related to their strengthening effect. Up to peak ageing, the ductility is reduced, while it increases again after peak ageing (Liu et al. 2004). The same trend has been observed for the toughness (Dumont et al. 2003). Shen et al. (2013) and Petit et al. (2019) observed Mg_2Si particles as the prime nucleation site in compact-tension specimens of an AA6061-T6 alloy, while the (Fe,Si)-rich particles cracked at higher strains. Nucleation of voids at constituent particles only at very high strains was also observed by Ghahremaninezhad and Ravi-Chandar (2012) in tensile tests of a 6061-T6 alloy.

For thin sheets, the Kahn tear test (ASTM Standard B871-01 2001) gives a good comparative measure of the fracture toughness for aluminium alloys in accordance with other fracture toughness measures (Dumont et al. 2003). Remote mode I tearing of thin metal sheets normally results in either a flat (cup–cup) fracture mode or a slant fracture mode (fully slant or V-shaped/cup-cone). Traditionally, the fracture mode has been correlated with the hardening capacity. Pardoen et al. (2004) showed that a number of materials with high strain hardening capacity in common systematically fractured in a flat manner. Hickey and Ravi-Chandar (2016) studied an O-temper and a T6-temper of a 6061 alloy, which respectively fractured in a flat and a slant mode. Some authors have further connected the strain hardening capacity that decides the local fracture mode to depend on the particle content. Tekoğlu and Nielsen (2019) and Çelik et al. (2021) modelled particles discretely in a 2D plane-strain model and found that the number, size, distribution and shape of the particles strongly influence the resulting tearing mode. For high numbers or large sizes of the nucleation sites, the damage mechanism shifts from void-by-void interaction, causing cup–cup fracture, to simultaneous interaction of multiple voids, causing slant fracture. These mechanisms were also distinguished and respectively associated with lower and higher inclusion volume fractions by Srivastava et al. (2014). Bron et al. (2004) observed experimentally that dispersoids were involved in the fracture mechanism between the primary voids in the slant part of the crack, while internal necking was dominant in the initial flat tunnelling at the notch. Tekoğlu and Nielsen (2019) also found that for low to intermediate contents of particles, macroscopic shear banding occurs before microscopic damage nucleation. Formation of shear bands preceding void nucleation was also observed experimentally by other authors for both a low and high work-hardening 2000-series aluminium alloy by the use of in-situ synchrotron laminography and digital volume correlation (Morgeneyer et al. 2014; Buljac et al. 2016, 2018). The shear bands formed occur in pairs, with the two bands normal to each other. One of the bands is active, but which band is active may alternate, such as seen using digital volume correlation by Buljac et al. (2016, 2018). In some cases the switch of active band results in crack flipping (El-Naaman and Nielsen 2013; Buljac et al. 2018). The shear band switches start by shear lips forming near the plate surface, which eventually merge to the opposite shear band (El-Naaman and Nielsen 2013; Nielsen and Gundlach 2017), and the switches may occur in a systematic manner, see, e.g., El-Naaman and Nielsen (2013).

This experimental work is focused on the effect of the constituent particles on the mode I tearing behaviour of three cast and homogenized 6000-series aluminium alloys. By increasing the amounts of Fe and Si, we aim to achieve a second version of the alloys with higher constituent particle content. The goal is to get two versions of each alloy with different ductility, while retaining the strength level. By carefully controlling the chemical composition, we try to isolate the effect of increased constituent particle content on fracture and crack propagation in Kahn tear tests and relate these findings to previous observations on the effects on the tensile ductility. Detailed studies on the tensile ductility of these alloys were performed by Thomesen et al. (2020) and Tomstad et al. (2021), except for one of the alloys studied here. A summary of these results is presented in Sect. 2 of this paper, which is further organized as follows. The experimental program and data acquisition procedures are briefly presented in Sect. 3. Section 4 provides the results, which are discussed in Sect. 5. Concluding remarks are presented in Sect. 6.

2 Materials and experimental background

In this work, we investigate three 6000-series aluminium alloys. Two versions of each alloy are studied; one is a commercial alloy, while the other is tailored to have a significantly higher content of constituent particles while retaining the same yield strength and work-hardening. The three commercial alloys are AA6061, AA6063 and AA6110. In the following, the commercial alloys are referred to as alloy 6xxxA, while the tailored alloys are denoted alloy 6xxxB.

Characterizations of the microstructure and macroscopic stress–strain behaviour have been reported by Thomesen et al. (2020) for the three commercial alloys. Tomstad et al. (2021) extended the work for two of the tailored alloys, i.e., the alloys 6063B and 6110B, and compared them to the respective commercial alloys. A brief description of the particle characterization and tension test results from these studies are presented below for completeness, along with additional data for the 6061B alloy which have not previously been presented. For further details, the reader is referred to Thomesen et al. (2020) and Tomstad et al. (2021)[1].

2.1 Chemical composition and heat treatment

The B-alloys were designed to have a higher content of constituent particles than the A-alloys, while keeping other microstructural features unaltered. The aim was to retain the strength and work-hardening of the commercial alloy while observing the effect of the increased constituent particle content on the ductility and toughness. The higher constituent particle content was achieved by increasing the amount of iron (Fe) and silicon (Si) in the alloys. This is readily seen as the major differences between the A- and the B-alloy in Table 1, which presents their chemical compositions.

All six alloys were received (from Hydro Aluminium R&D Sunndal) as DC-cast extrusion billets in the cast and homogenized condition. A dendritic grain structure with equiaxed grains, typical for cast alloys, was found for all alloys. The average grain sizes are presented in Table 2. For the A- and B-versions of 6063 and 6110, the average grain size is similar, while some difference is seen for the two versions of 6061. It is however worth noticing that the two 6061-alloys have significantly larger grains than the other alloys, especially for the A-alloys where the size is nearly twice the grain size of the 6063- and 6110-alloys.

The various tensile test specimens were machined from the billets and then heat treated to temper T6 according to the following procedure:

- Solutionizing at 560 °C for 10 min followed by water quenching.
- Storage at room temperature for 24 h.
- Artificial ageing at 185 °C for 8 h followed by water quenching.

2.2 Particle content

The constituent particles were characterized through backscatter electron micrographs obtained using a scanning electron microscope (SEM). The cast and

[1] By a mistake, the original paper by Tomstad et al. (2021) contains data for a 6110B-alloy that had not been homogenized after casting. Note that the current paper presents data for the homogenized version.

Table 1 Chemical composition of the alloys (in wt%)

Alloy	Mg	Si	Fe	Cu	Mn	Zn	Ti	Cr	Al
6061A	0.903	0.621	0.209	0.204	0.038	0.054	0.106	0.060	Bal.
6061B	1.017	0.811	0.766	0.189	0.040	0.053	0.116	0.071	Bal.
6063A	0.470	0.512	0.206	0.001	0.047	0.003	0.006	0.001	Bal.
6063B	0.481	0.692	0.753	0.001	0.048	0.004	0.015	0.005	Bal.
6110A	0.828	0.720	0.196	0.203	0.506	0.003	0.026	0.157	Bal.
6110B	0.793	0.925	0.749	0.204	0.503	0.005	0.029	0.183	Bal.

Table 2 Average grain size, area fraction of constituent particles and the area-weighted average of the particle diameter in the alloys

	Average grain size (μm)			Area fraction of particles (−)			Average particle diameter (μm)		
	6061	6063	6110	6061	6063	6110	6061	6063	6110
A-alloy	124	63	67	0.0050	0.0061	0.0076	1.16	1.64	1.85
B-alloy	101	58	72	0.0172	0.0198	0.0240	1.45	1.67	1.60

Some of the data have previously been presented in the papers by Thomesen et al. (2020) and Tomstad et al. (2021)

homogenized condition causes a heterogeneous distribution of particles, with the particles situated on the grain and dendrite boundaries (Westermann et al. 2014). The images were post-processed to obtain the particle size distributions of each alloy, and the results are plotted in Fig. 1. The figure presents the fraction (in %) of the total constituent-particle area versus the equivalent particle diameter, the latter being defined as the diameter of a circle with the same area as the actual particle. Particles with an equivalent diameter less than 0.2 μm were omitted to avoid analyzing dispersoids. It is noted that only the two 6110-alloys contain dispersoids. The area-weighted average particle sizes of the alloys are presented in Table 2.

Table 2 and Fig. 1 show that the A-alloys have quite different particle size distributions. Alloy 6061A has a large fraction of smaller particles and a small fraction of larger particles, while the opposite is true for 6110A. The particle distribution of 6063A is intermediate. For 6063, the B-alloy has more or less similar size distribution and average particle size to the A-alloy, while a shift towards larger particles is seen for the B-alloy of 6061. This is in contrast to 6110, where a shift towards smaller particles is seen for the B-alloy relative to the A-alloy.

It should be noted that the number of particles in every size group varies significantly between the alloys, and that the figure only reveals information regarding the size distribution. The resulting area fractions of constituent particles are presented in Table 2. There is clearly a significant difference between the three A-alloys in terms of total particle content. The table also reports an approximately three times higher area fraction for the B-alloys than for the A-alloys, as was intended.

2.3 Tensile tests

Tensile tests on axisymmetric smooth and notched specimens have been performed for the A- and B-versions of the three alloys. All specimen geometries had a nominal gauge diameter of 6 mm, and the notched specimens had nominal notch radius of 2.0 mm and 0.8 mm.

Figure 2 shows the true stress–logarithmic strain curves obtained from the tensile tests. These are average measures across the minimum cross section. The true stress σ was calculated as $\sigma = \frac{F}{A}$ and the logarithmic strain ε was calculated as $\varepsilon = \ln \frac{A_0}{A}$, where F is the measured force, A_0 and $A = \frac{\pi}{4} D_1 D_2$ are the initial and current cross-sectional area, respectively, based on two perpendicular laser gauge measurements of the diameter of the specimen D_1 and D_2. Alloys 6061 and 6110 have similar strength, which is markedly higher than for 6063. Simulations using the nanostructure model NaMo (Myhr et al. 2015) were presented by Thomesen (2019) for the A-alloys. The results showed that the

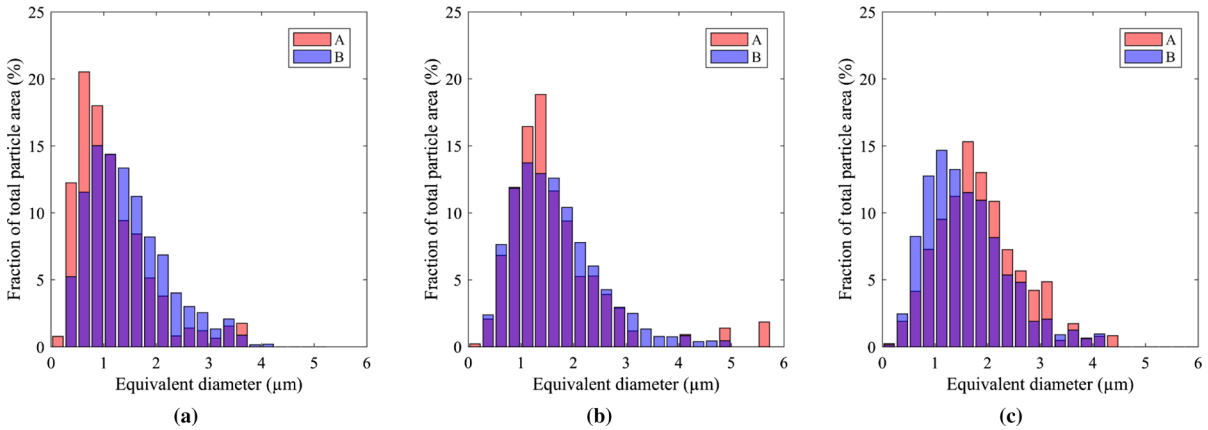

Fig. 1 Particle size distribution plots for the A and B versions of the three alloys: **a** 6061, **b** 6063 and **c** 6110. Some of the data have previously been presented in the papers by Thomesen et al. (2020) and Tomstad et al. (2021)

lower strength of 6063A was due to a somewhat lower precipitate level and a markedly lower solute level in this alloy compared to the two other A-alloys. Figure 2 further shows that the corresponding A- and B-alloys display fairly similar strength, with only minor differences in the stress level for 6061A and 6061B and for 6110A and 6110B, while 6063B has stress levels somewhat above 6063A. It is however noted that the stress–strain curves are plotted from just below the yield stress, and thus rather small differences seem pronounced. The small increase in strength is attributed to a small amount of the extra Si not forming constituent particles with Fe as intended, but rather forming hardening precipitates with excess Mg, or by some amount of Si or Fe remaining in solid solution and thereby contributing to the solid solution hardening. Only minor differences in the slope of the work-hardening curve are observed.

The failure strain of the B-alloys is notably reduced compared to the A-alloys. The alloys 6061A and 6063A have comparable failure strains for all geometries. The comparable ductility was found despite nearly twice as large grains and a significantly higher yield stress for 6061A than for 6063A, which was attributed mainly to the large portion of smaller-sized constituent particles (and the lower constituent-particle content overall) in 6061A (Thomesen et al. 2020). Further, 6061B appears to be more affected by the increased constituent-particle content than 6063B. The stronger effect of increasing the constituent-particle content found for 6061B is presumably due to the shift towards larger particles, while the particle size distribution of 6063B is almost unaltered compared to 6063A. Although the grain size is somewhat smaller in 6061B than in 6061A (while being similar for the two 6063-alloys), the shift towards larger particles in 6061B is seemingly of greater importance for the ductility of this alloy. Alloy 6110A has lower failure strains than the the other A-alloys, which is attributed to the high strength and larger particle sizes (Thomesen et al. 2020). The failure strain of 6110B is also significantly lower than those of the other B-alloys. However, 6110 is less affected by the increase in constituent particle content than 6061. This is attributed to the shift towards smaller particles for 6110B, while the particle size distribution shifts towards larger particles for 6061B.

Introducing a pre-machined notch reduces the failure strain of all the materials due to the increased stress triaxiality in the notch region. However, the failure strain does not strictly decrease with decreasing notch radius, as would be expected, and the failure strain of the R0.8 tests is either nearly equal to or larger than for the corresponding R2.0 tests for all six alloys. Thomesen (2019) investigated this observation using finite element simulations, and found that fracture initiated at different locations for the two geometries. Damage accumulation is known to be driven by the plastic strain, but amplified by the stress triaxiality. The large differences in the stress triaxiality versus plastic strain curves of the R2.0 and R0.8 specimen geometries were thus leading to different failure modes, which is a viable explanation to this unexpected observation. The reader is referred to that work for details.

The notch sensitivity, defined by the relative reduction in failure strain of a notched specimen compared to

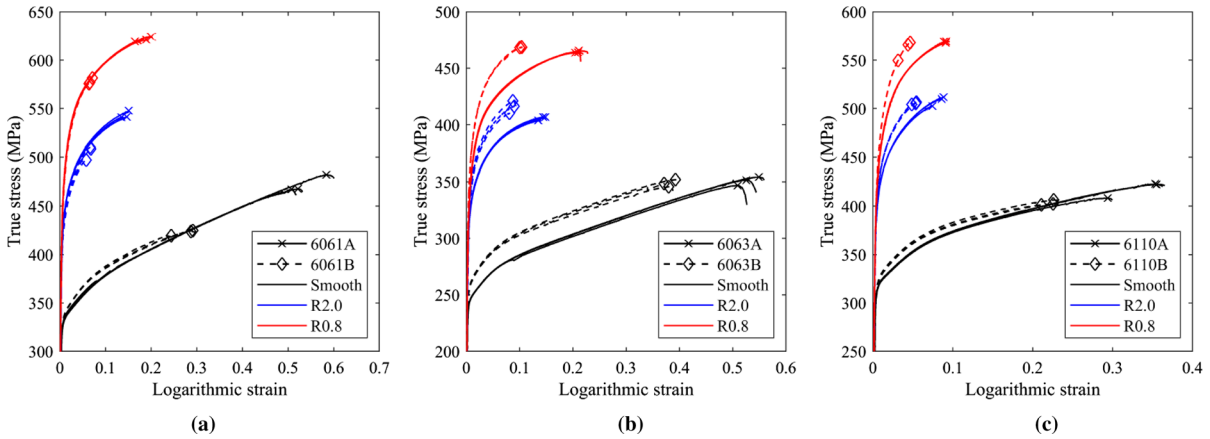

Fig. 2 True stress–logarithmic strain curves from tensile tests on smooth and notched specimens of **a** 6061, **b** 6063 and **c** 6110. The markers indicate the point of failure, defined as when the true stress starts to decrease. The curves are obtained from raw data also used by Thomesen et al. (2020) and Tomstad et al. (2021)

the smooth specimen, is notable for all alloys. For the B-alloys, the notch sensitivity is fairly constant throughout the selection of alloys and notch radii. The same is true for the A-alloys, except for the R0.8 specimens of 6061A and 6063A which display a markedly lower notch sensitivity than the remaining specimens of the A-alloys. Although the level of the notch sensitivity is somewhat similar for the A- and B-alloys, there is a slight, but consistent, increase in notch sensitivity of the B-alloys relative to the A-alloys. The difference in notch sensitivity between the A- and B-alloys is small compared to the overall reduction in ductility, and is hence not considered a main outcome of the increased constituent particle content, but the difference in the failure strain between the A- and the B-alloys is somewhat larger for the notched specimens, and in particular the R0.8 specimens, than for the smooth specimens.

The reader is referred to Thomesen et al. (2020) and Tomstad et al. (2021) for a more detailed presentation of the tensile tests of all alloys except alloy 6061B, for which the results have not been published before.

2.4 Summary

The relevant main findings from the tensile tests and previous studies (Thomesen et al. 2020; Tomstad et al. 2021) are as follows:

- Alloys 6061 and 6110 have a similar strength, while alloy 6063 has a lower strength due to its lower precipitate content and solute levels.
- Alloy 6063B has a slightly higher strength than alloy 6063A, presumably due to some of the added Si precipitating with Mg or the additions contributing by solid solution hardening.
- Alloys 6061A and 6063A have a similar ductility, while alloy 6110A has a lower ductility. The trend in ductility for 6063A and 6110A is presumably strongly related to the strength. The remarkably high ductility of 6061A is attributed to the higher fraction of smaller particles than for 6063A.
- The ductility is more reduced for 6061 than for 6063 and 6110 between the A- and B-alloys, which is mainly attributed to a shift towards a larger particle size, while 6063 retained a similar particle size distribution for B as for A and 6110 had a shift towards smaller particles for B.

3 Experimental methods

3.1 Kahn tear test specimens

The specimens were produced by wire erosion according to the geometry specified in ASTM Standard B871-01 (2001), with the exception of the notch radius, which, due to limitations in the applied fabrication method, had to be increased. The standard specifies a

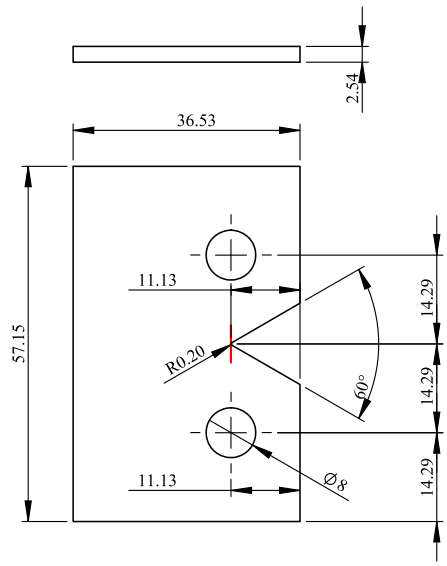

Fig. 3 Nominal specimen geometry. Dimensions are in mm. The vertical red line across the notch root represents the virtual extensometer applied in the DIC analyses

Table 3 Measured notch radii for the various test series

	6061	6063	6110
A-alloy	0.24 mm	0.21 mm	0.20 mm
B-alloy	0.20 mm	0.20 mm	0.18 mm

notch radius of 0.00025 in. (0.006 mm), while the nominal radius here is 0.2 mm. The contour of the geometry was first machined, before slices in the desired thickness were cut from this piece. Hence, the notch root is equal for all the specimens of each alloy. The nominal geometry is shown in Fig. 3. The specimens were heat treated after machining to temper T6 according to the procedure specified in Sect. 2.1.

The initial notch radius was checked using edge tracing with the in-house Digital Image Correlation (DIC) software eCorr (Fagerholt 2017), and is presented for all the alloys in Table 3. It is noted that the observed deviations in notch radius may affect the initiation of the crack in the tear tests.

3.2 Test setup

The tear tests were performed in Instron 5900-series universal testing machines at a crosshead velocity of 1 mm/min. The force and the crosshead displacement were logged by the machine at 10 Hz. Six tests of each material were carried out. Two of the tests for each material were run until the force was down at 2% of the peak force, while the remaining four tests were stopped at 80, 60, 40 and 20% drop from the peak force. Two Ximea CB200MG-CM 20 megapixel cameras, placed on each side of the specimen, captured the deformation on the surface of the specimen. There was also a lamp on each side to illuminate the specimen. For most of the tests, the frame rate was 1 Hz, while for some tests the frame rate was increased to 3 Hz. The latter applied to those tests of the B-alloys that were stopped prior to a complete drop in force.

The specimens were attached to the machine with clevises and pins, together with 3D-printed plastic spacers occupying the gap between the specimens and the clevises to restrict lateral movement. The specimens were painted with a black-on-white speckle pattern before testing to prepare for DIC analysis.

3.3 Digital image correlation (DIC)

2D-DIC with the in-house software eCorr was used on the image series to obtain displacement data by a virtual extensometer and strain field plots. DIC analyses were mainly run only on the image series from one side of the specimens, but were for some tests run on the image series from both sides of the specimens, to check that this gave only small differences in the response curves.

An element size of approximately 0.4 mm was used in the DIC analyses. Elements were eroded as they reached a critical element strain to avoid problems with the image correlation. The critical strain was chosen for the element erosion to best fit the crack propagation of the image series at hand. To obtain alternative displacement data to the crosshead displacement, a 6 mm virtual extensometer was placed just across the notch tip of the initial images, see Fig. 3. The virtual extensometer was used to measure the notch opening displacement (NOD).

3.4 Computed tomography (CT)

After testing, the unloaded specimens were CT scanned in a Nikon XT H225 ST MicroCT machine at the X-ray laboratory at the Department of Physics, NTNU.

The scans were reconstructed using Nikon CT Pro 3D, versions XT 4.4.2/3, reporting a voxel size of 19–25 μm. For the first specimen series that was scanned, which was 6061A, the specimens were scanned one by one, while the remaining series scanned the entire series at once. The programmes ImageJ 1.52a (Rasband 1997–2018) and ParaView 5.7.0-RC1 (Ahrens et al. 2005) were used for visualization, i.e., to study slices in three orthogonal directions and to render 3D models of the fracture surfaces, respectively.

3.5 Scanning electron microscopy (SEM)

The fracture surfaces of the tested Kahn specimens were investigated from secondary electron images obtained using a Zeiss Gemini SUPRA 55VP Field Emission Scanning Electron Microscope (FESEM) operated at 15 kV. To access the fracture surfaces, the specimens were carefully cut to separate the specimen halves. All specimens were cleaned in an ultrasound bath using acetone, before inserted into the vacuum chamber of the FESEM.

4 Results

4.1 Response curves

The force–notch opening displacement (NOD) curves obtained from the elongation of the virtual extensometer are shown in Fig. 4 for each of the alloys, while Fig. 5a and b show the force–crosshead displacement curves for the two complete tests for all the A- and B-alloys, respectively. These curves are further used to calculate the unit initiation energy (UIE) and the unit propagation energy (UPE), respectively, both found in Table 4. The UIE was calculated as the area below the force–NOD curves up to the point of maximum force, divided by the original net area of the specimen. It is stressed that the UIE might be affected by differences in the notch radius between the test series, see Table 3. The UPE was found as the area below the force–crosshead displacement curves of the two complete tests from the maximum force and until the end of the curve, divided by the original net area of the specimen. The UPE is hence only computed for the two tests in each series that were run until 2% of the maximum force.

The tests on the A- and B-alloys were performed on two different occasions, using two different, but intentionally equivalent machines. The slope of the force–crosshead displacement curves for the A-alloy tests and the B-alloy tests were compared to evaluate the equivalence of the two setups. After an initial deviation the slopes were not distinguishable, indicating a comparable machine stiffness after the initial specimen-to-fixture alignment. As the virtual extensometer coincides with the force axis before crack propagation, its data can be used for computing the UIE. In this way we avoid any inaccuracies on this measure originating from using the crosshead displacement, and in particular from using two different machines for the A-alloy tests and the B-alloy tests. As the crack opens, the virtual extensometer will shift with respect to the force axis due to rotation of the specimen halves about the pins, and the virtual extensometer can no longer be used to calculate the energy. The comparable machine stiffness suggests that calculating the UPE from the crosshead displacement should be acceptable, as the specimen and fixtures should be well set from the point of crack initiation and onwards.

For all alloys there is a clear effect on the response curve in Fig. 4 of the increased constituent-particle content. Owing to the reduced ductility, but comparable strength, the peak of the curve is reached earlier and is hence lower and sharper, which represents less necking and a more abrupt fracture. The peak force for 6063 is less affected than the peak force for 6061 and 6110. The response curves deviate little before the peak. The peaks of the response curves of 6061B, 6110A and 6110B are more scattered than those of the other alloys, and there is some more scatter in the response curves of 6110 than in those of the other alloys.

As can be seen in Table 4, alloy 6061A has the highest UIE, which is attributed to its superior combination of strength and ductility, but the slightly larger notch radius could also contribute. The UIE of alloy 6063A is not much below, despite its lower strength and the lower peak in the response curves. However, for 6063A the peak occurs at a moderately higher displacement in the response curves than for 6061A, which partly compensates for the lower peak force. The UIE is notably lower for 6110A than for the other two A-alloys, due to the much lower ductility of this alloy. For 6061 and 6110, the UIE is reduced by approximately 60% for the B-alloy with a higher constituent particle content com-

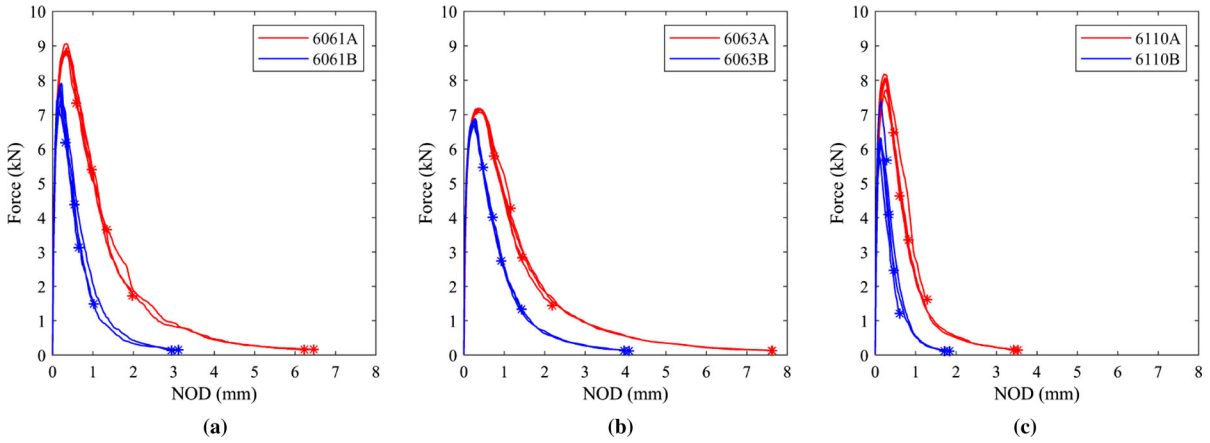

Fig. 4 Force–NOD curves from the Kahn tear tests, where the NOD was measured by DIC using a virtual extensometer with a 6 mm gauge length placed across the notch: **a** 6061, **b** 6063 and **c** 6110. The points where the tests are stopped are marked with asterisks

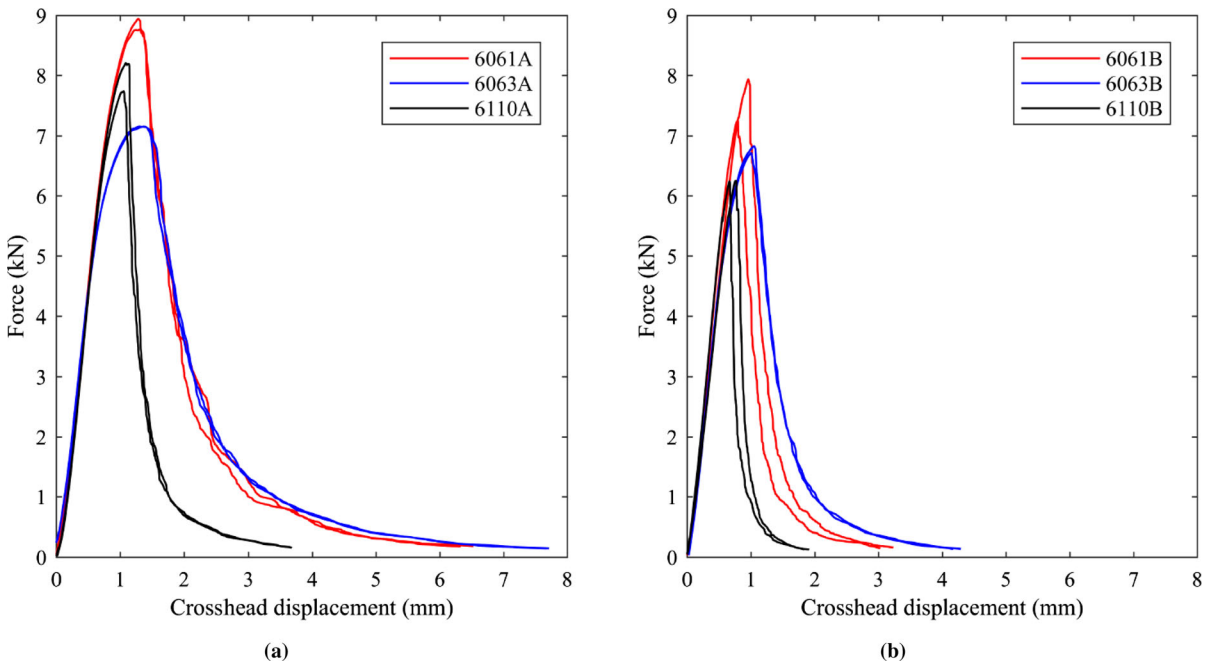

Fig. 5 Force–crosshead displacement for the two tests of each of the **a** A-alloys and the **b** B-alloys run to 2% of the maximum force

pared to the A-alloy. For 6063, the UIE is reduced by about 40% for the B-alloy compared with the A-alloy.

The UPE is similar for 6061A and 6063A, despite the peak force being much higher for 6061A than for 6063A, see Fig. 5. The longer tail of the response curve for 6063A and its marginally shallower slope compensate for the difference in the peak force on the resulting UPE. Alloy 6110A has a much lower value of the UPE than the other two A-alloys, which is related to the steep drop in the response curve at after the peak force, see Fig. 5a. The relative difference in UPE between the A- and B-alloys is similar for 6061 and 6110, with a reduction by two thirds from the A-alloy to the B-alloy, while for 6063 the UPE is approximately halved.

Table 4 Unit initiation energy (UIE) and unit propagation energy (UPE)

Alloy	UIE (kJ/m^2)	UPE (kJ/m^2)
6061A	37.9 ± 2.6	117.3, 124.2
6061B	16.2 ± 2.0	41.9, 42.8
6063A	35.7 ± 1.1	125.5, 121.2
6063B	22.2 ± 1.2	55.0, 59.9
6110A	24.4 ± 2.6	46.1, 46.9
6110B	9.8 ± 1.4	17.1, 16.0

The UIE is presented as the average and the standard deviation of all six tests. The UPE is presented as each measurement of the full tests

4.2 Strain fields

Most of the Kahn tear tests exhibited a steady slant fracture throughout the entire crack propagation after a flat-to-slant transition. The fracture mode was clearly visible in the DIC strain fields as a strain concentration on the surface that is wider on one side of the crack than on the other side. An example on how the effective strain field typically develops as the crack advances is shown in Fig. 6, where the strain field of one of the 6063A tests is plotted. This material has more intense strains than the others, and hence shows most clearly the observed trends. Before the crack initiates, a "butterfly-wing shaped" strain field (Frodal et al. 2020) can be seen at the notch (Fig. 6a). The crack then initiates in one of the wings, typically reversed on each of the sides of the specimens, such that a slant crack forms after the initial crack shape. The shape of the crack will be covered in more detail in Sect. 4.3, where the CT results are presented. For the initial part of the crack propagation (Fig. 6b, c), the strain field around of the crack tip is of a lower intensity and more blurred than what proceeds (Fig. 6d, e). As the crack approaches the back of the specimen, the response curve flattens out, the crack propagation is limited, and most of the deformation is compression of the back of the specimen. At this point, the strain field around the crack tip becomes less pronounced again, see Fig. 6f and g for 6063A.

Figure 7 shows the effective strain field at the end of the test for one specimen of each material. For all materials, slant strained bands are observed, which are oriented between the loading direction and the direction of crack propagation. There are clearly higher intensity strains around the crack for 6063 than for 6061 and 6110, and for 6110 the deformation outside of the cracked region is limited. In all three cases, the strains in the specimens of the B-alloy are considerably reduced with respect to the corresponding A-alloy.

4.3 Computed tomography scans

Studying the CT scans did not reveal any differences in the overall fracture mode between the alloys, as all tests failed by slant fracture. Figure 8 shows a render of the CT scan of all the specimens from one test series. The initial tunnelling results in a flat triangular region (Bron et al. 2004; Morgeneyer et al. 2010) on the fracture surface, with shear lips towards the specimen surface. This region can be seen at the notch tip of the tests in Fig. 8. As the crack progresses, the shear lips grow and merge. In most cases, the shear lips are in the same direction, and merge to form a slant fracture. This is commonly referred to as a flat-to-slant transition. However, in some tests, the shear lips form in opposite directions, merging to a V-shaped fracture mode after the flat triangular region. In all these tests, one of the halves of the crack eventually flips to the other shear band, continuing as a slant fracture. In some cases, this happens already in the initial stage, before the shear lips merge.

The slant crack that forms has an angle of approximately 45°. The crack tends to have a slight S-shape, as shown by Fig. 9a for 6063B, but is sometimes more planar, as illustrated for 6110B in Fig. 9b. This shape change appears to have a slight correlation with the ductility of the alloy, but this connection is somewhat diffuse and the shape even varies within each test. Along the crack propagation, the fracture surface shows some roughness, particularly in the centre. An example is shown in Fig. 9c, but this is also clearly visible in Fig. 8. Some partial flipping to opposite shear bands also occurs from the surface of some specimens, as shown in Fig. 9d, but the crack never flips completely, and eventually it flips back. In some of these cases, cracking is visible in both shear bands simultaneously. One case is illustrated in Fig. 9e, where it may be spotted on the left side of the specimen.

Despite limited resolution of the scans, an indication of tunnelling of the crack can be observed by the crack being visibly open in the middle, while appearing closed towards the surface. This is shown in Fig. 9f, where edges on the surface can also be seen, indicating shearing towards the specimen surfaces. Also Fig. 8 illustrates the occurrence of tunnelling clearly.

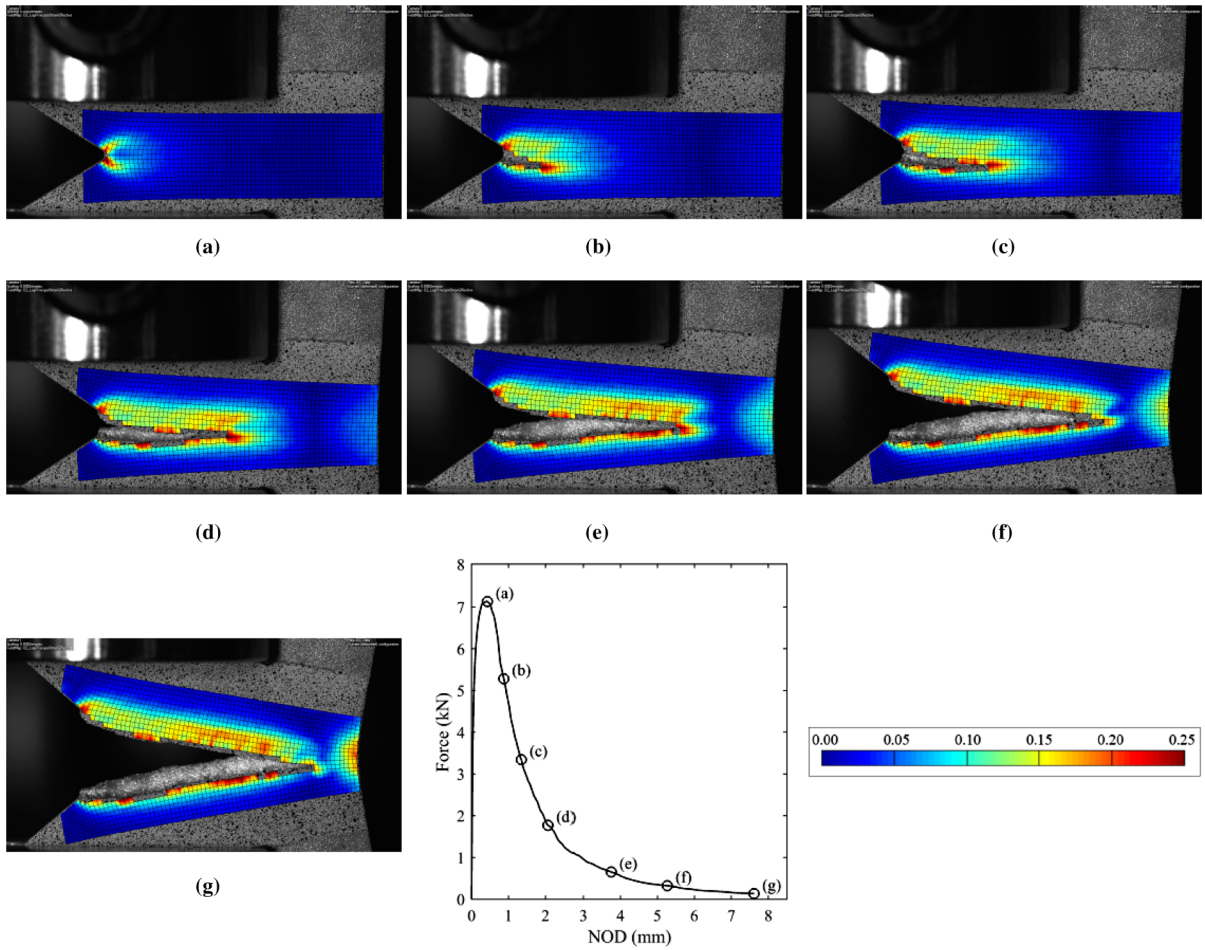

Fig. 6 Effective strain field of 6063A during crack propagation, where the sub-figures **a**–**g** correspond with the respective labels in the force–NOD curve

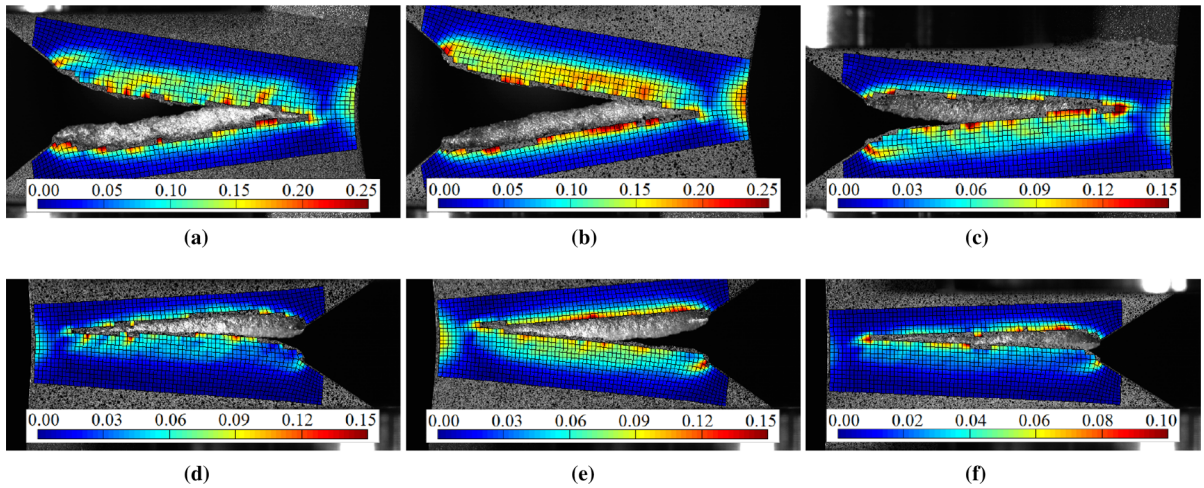

Fig. 7 Effective strain field at 98% drop from peak force (end of test) for all materials: **a** 6061A, **b** 6063A, **c** 6110A, **d** 6061B, **e** 6063B and **f** 6110B. Note that the colour legend is scaled differently for each material

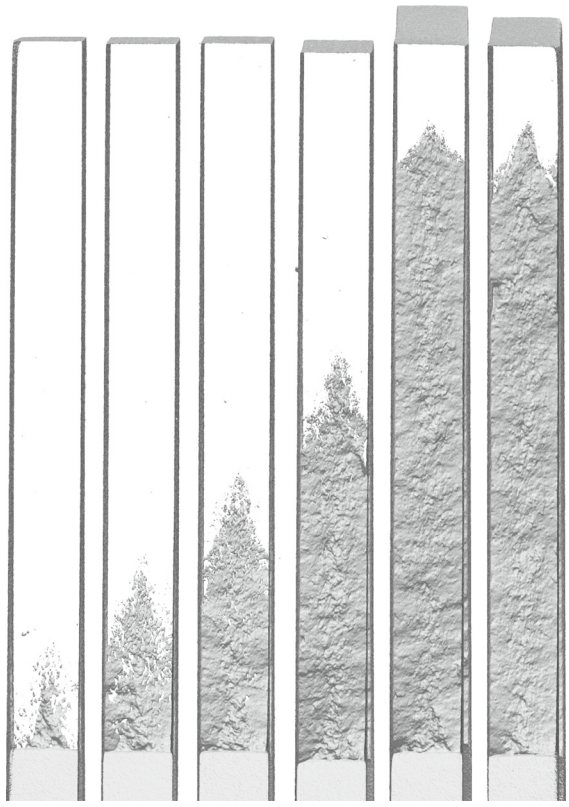

Fig. 8 Rendered CT scan of the test series of 6061B. From left to right: stopped at 20%, 40%, 60%, 80% and 98% (two repetitions) drop from peak force. Due to limited scanning resolution and unloading before scanning, the render is not capable of capturing the crack tip perfectly

Again, due to the limited resolution, a very small distance between the two crack faces and elastic unloading, the crack tip must not be interpreted as perfectly represented, but the figure shows that the crack is more opened in the centre than towards the specimen surface close to the crack tip. It is noted that it has been shown in the literature that the tunnelling effect in slant cracks is certainly limited compared to the tunnelling effect in flat cracks or in the initial flat tunnelling (James and Newman Jr. 2003; Bron et al. 2004).

Any particular behaviour at stages in the crack propagation was not found in the CT scans. Only the "fully" propagated cracks differed from the cracks that were stopped intermittently, as they were more opened and the thickness at the crack tip was close to the thickness of the undeformed parts of the specimen. This observation corresponds with the DIC strain field evolution during the crack growth, where there was little strain immediately ahead of the crack tip of the fully propagated cracks. The thinning of the specimen at the crack tip shows little variation until the crack enters into the compression region of the specimen. The thickness of the specimen at the last point where the crack tip is detectable in the scans, varies between the alloys from approximately 84% for 6063A to approximately 97% for 6110B compared to the thickness of the specimens outside of the necked region, with the other alloys between these limits. Figure 9f and g show the necking of 6063A and 6110B specimens at the location of the very last visible sign of the crack, illustrating the substantial difference in ductility between these two alloys. In general, the trends in the thinning correspond well with the trends in tensile ductility between the alloys observed in Sect. 2. Beyond the differences in the thickness reduction and the opening of the cracks, no systematic differences were found between any of the alloys in the CT scans.

The slant strained bands observed in the DIC results were observed as out-of-plane deformation at the surface of the specimens in the CT scans, as illustrated in Fig. 10a and b, and appeared often to coincide with an uneven crack edge, e.g., small instances of incipient flipping at the edge of the crack, see Fig. 10c. The example shown in Fig. 10 had a very intense strained band. As may be seen approximately in the centre of the CT scan rendering and the SEM imaging in Fig. 10d and e, respectively, there is a "roof shape" on the fracture surface. This is the incipient flip continuing from the edges towards the centre, in the crack propagation direction. However, it quickly turns back to the original band, and the crack continues as before the partial flip.

4.4 Fractography using scanning electron microscopy

The microscopic dimple structure of the fracture surfaces from the Kahn tear tests was investigated by means of SEM images. From the CT study, it was found that a flat triangular zone occurs at the crack tip (i.e., in the initial tunnelling region) with a surface normal to the loading axis and shear lips on the sides towards the edges of the specimen. The flat triangular zone typically transitions into a slant fracture which is the preferred fracture mode in all of the tests.

The flat triangular zone shows a classic dimple structure with mostly coarse dimples having a diameter of approximately 5–25 μm. Examples of the general

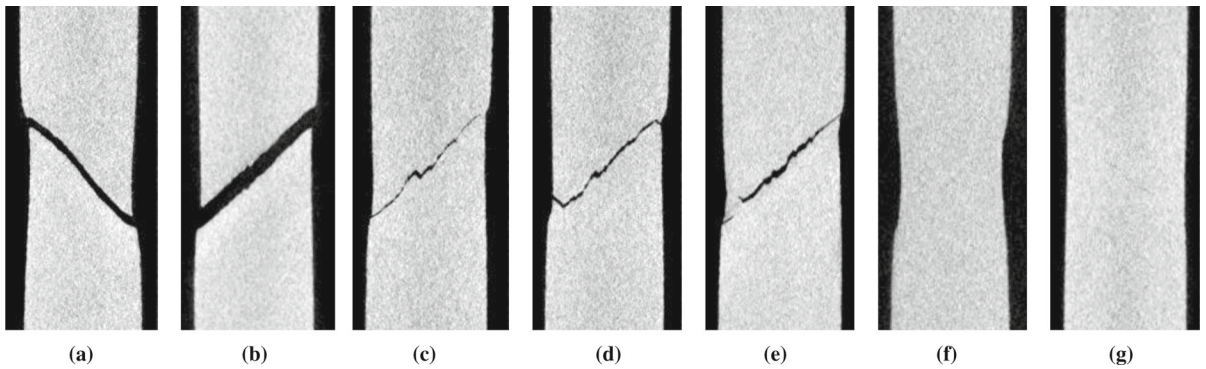

Fig. 9 A selection of examples on miscellaneous crack behaviour from the CT scans: **a** slight S-shape of the slant fracture, **b** planar slant fracture, **c** non-smooth centre of the crack, **d** partial flipping of the crack on the specimen surface, **e** cracking in both shear bands, **f** edges formed on the surface at the location of the last faintly visible crack tip in a specimen from the series with largest thickness reduction, and **g** location of barely visible crack tip in a specimen from the series with lowest thickness reduction

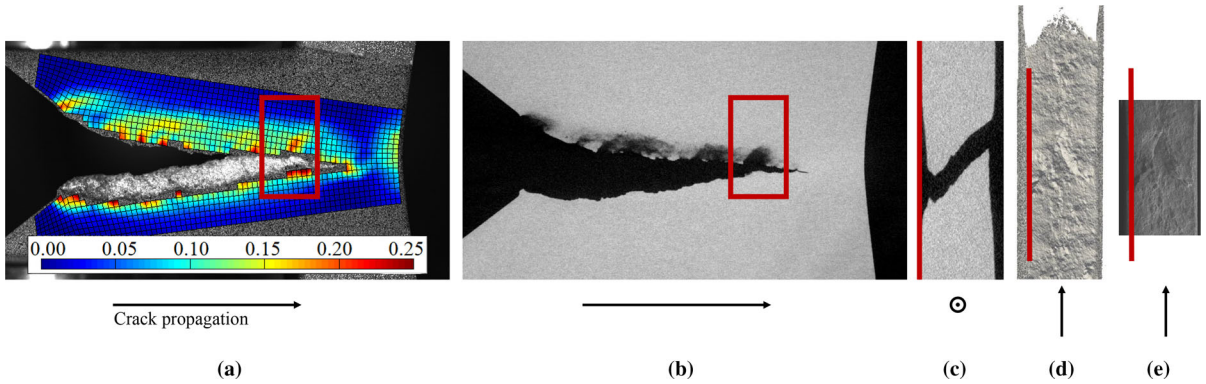

Fig. 10 Out-of-plane deformation close to the crack edge. **a** DIC strain field, **b** and **c** CT scan slices, **d** CT scan render and **e** SEM image. Arrows indicate the crack propagation direction

appearance are shown in Fig. 11a and b for alloy 6063A and 6063B, respectively. Constituent particles are seen at the bottom of most dimples, indicating that fracture occurs by nucleation, growth and coalescence of voids at these particles.

The aforementioned fracture mechanism reveals a generally ductile fracture behaviour of all alloys. The shape of the dimples and the fracture mode indicate that the triangular zone experienced a tension stress state to fracture. These observations are valid for all A- and B-alloys; however, the average dimple size appears to be smaller for the B-alloys. Tomstad et al. (2021) found a greater tendency of clustering of constituent particles in the B-alloys than in the A-alloys, and thus the smaller dimple size in the B-alloys is attributed to the much higher volume fraction and smaller spacing of the constituent particles. The high density of constituent particles is clearly visible along the entire fracture surface, see examples for the alloys 6061A and 6061B in Fig. 11c and d, respectively. Although there are lots of particles visible for both alloys, there is generally a markedly higher density on the fracture surface of the B-alloy.

The CT scans revealed some surface roughness throughout the crack path, particularly in the centre of the specimen thickness. SEM investigations reveal a similar dimple structure in the centre-most part of the slant crack as in the triangular zone, indicating a tension-dominated stress state in this region. The low density of coarse dimples is found for all alloys in the

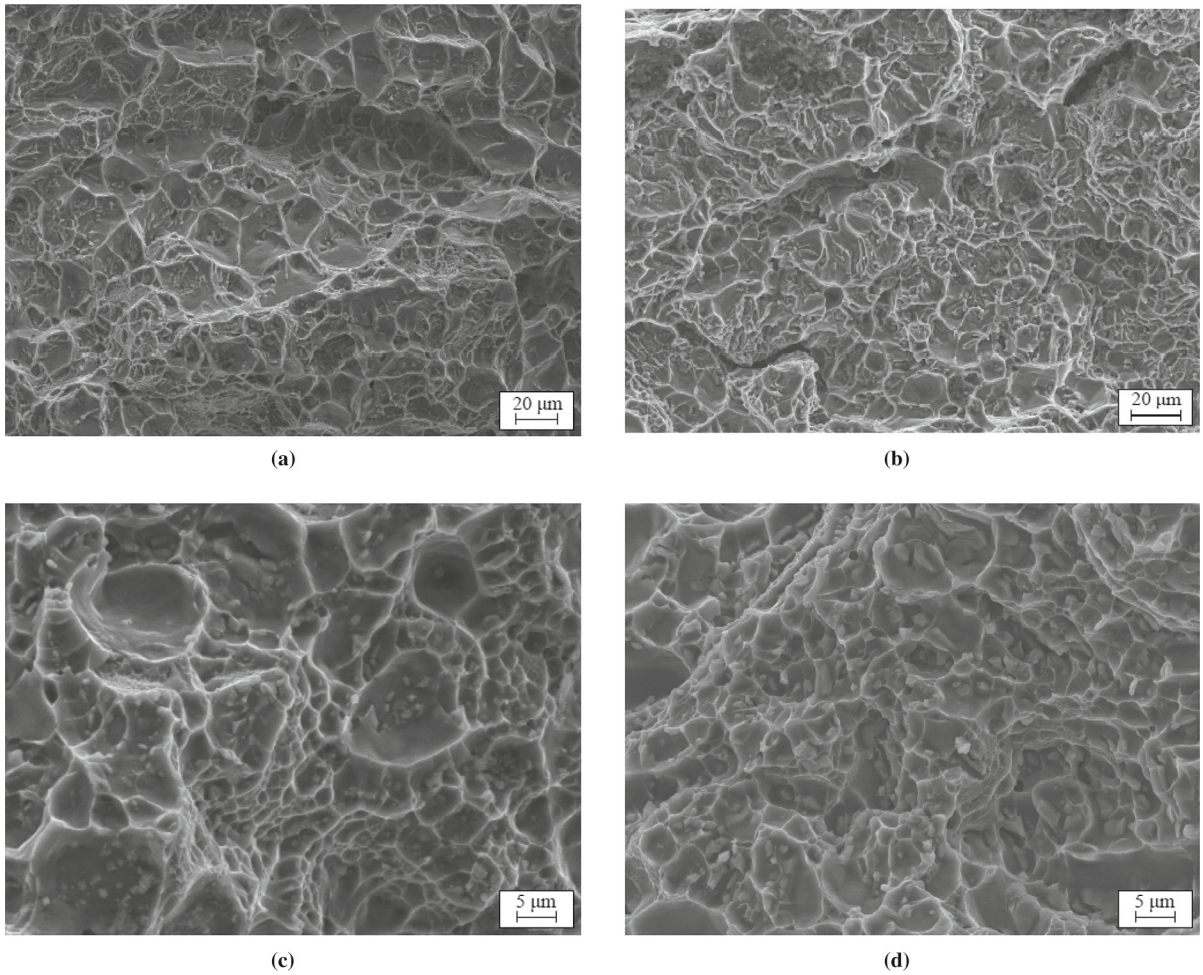

Fig. 11 SEM images of the fracture surfaces in the flat, triangular zone in **a** 6063A and **b** 6063B, and constituent particles on the general fracture surface of alloy **c** 6061A and **d** 6061B

centre region, with some differences in dimple size as described in the previous paragraph. In addition, there are areas in-between the coarse dimples that show a high density of tiny dimples, see Fig. 12a. This feature is especially prominent in the two 6110 alloys, but is also observed on the fracture surfaces of the two 6061 alloys. Intergranular fracture is markedly present on the fracture surface of alloy 6063A, which can be seen from Fig. 12b; however, this feature was not as prominent in alloy 6063B. The latter observation was also made by Tomstad et al. (2021) in tension tests on smooth and notched specimens of the extruded A- and B-alloys. For the two 6110-alloys it is possible to observe small dispersoids in the dimples, as shown in Fig. 12c.

Towards the edges of the slanted crack, the appearance of the fracture surface is completely different from the flat triangular zone, see the example given in Fig. 12d for alloy 6061A. Close to the edges of the specimens, there are relatively large areas without dimples that have either a rather smooth or a somewhat rough surface. Dimples are observed here as well, but these dimples have a more parabolic appearance. The clearly different appearance of the fracture surface compared with the flat triangular zone and centre-most part of the slant crack is caused by the different stress state in this area, which is more shear-dominated. There is obviously a transition between the extremities observed at the edge and the centre-most part of the crack, and in this transition zone a blend of the above features is

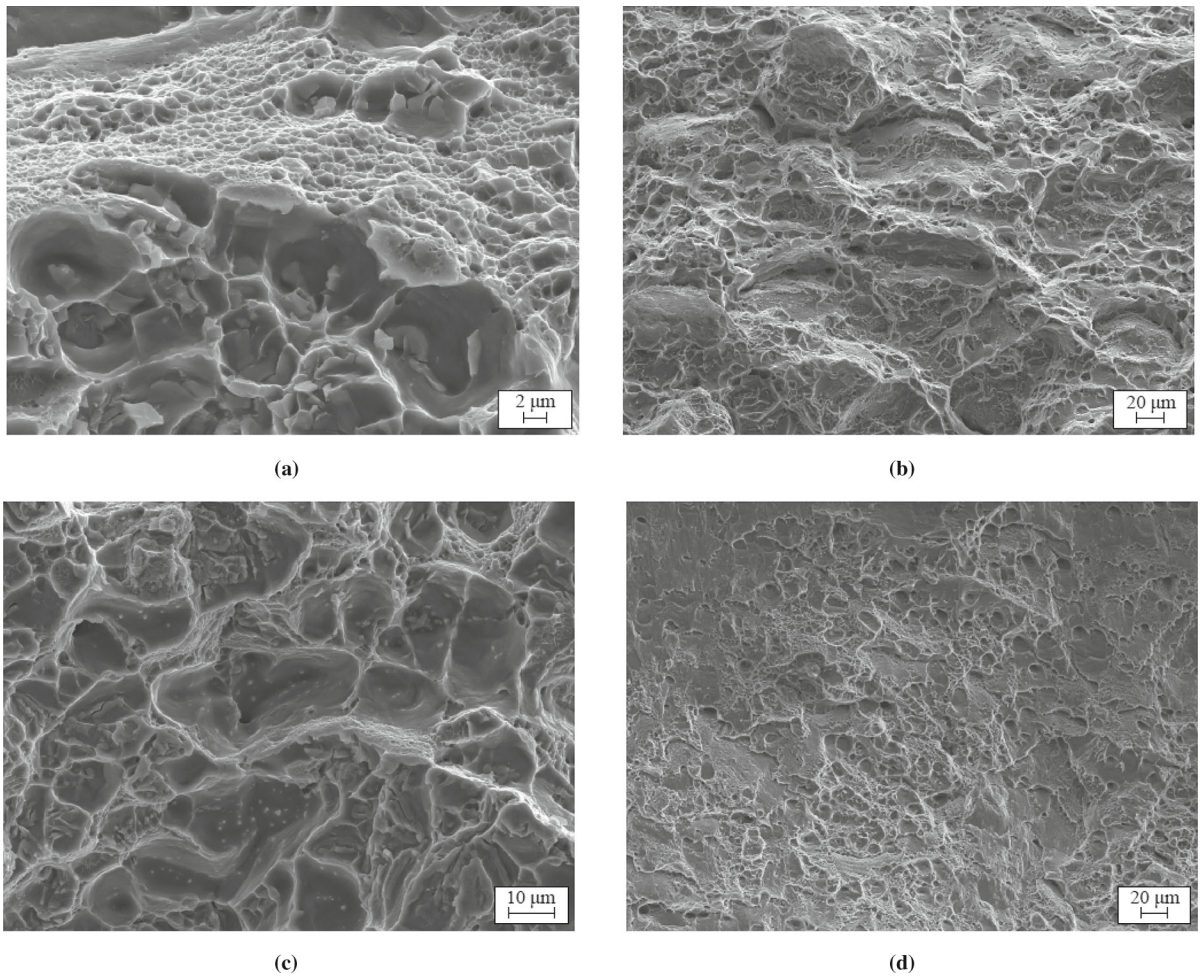

Fig. 12 SEM images of the fracture surfaces in the Kahn tear tests: **a** small and large dimples in 6110A, **b** intergranular fracture in 6063A, **c** dispersoids in 6110A, and **d** towards the edges of the slant crack in 6061A

found. This appearance of the fracture surface is found for all alloys; however, there are some differences in microscopic and macroscopic surface roughness and the extent of the smooth areas before and throughout the transition zone for the various alloys.

The above-mentioned observations from the fracture surfaces of the Kahn tear tests greatly resemble the observations made on fracture surfaces of axisymmetric tension tests performed by Thomesen et al. (2020) and Tomstad et al. (2021). A clear connection is seen between the fracture surface in the flat triangular zone and the centre-most region of the Kahn specimen to the centre part of the tension specimens, and also the slanted edges of the Kahn tests have many similarities to the shear lips near the periphery of the tension specimens. For the flat triangular zone and the centre-most region of the Kahn specimen, the size and shape of the dimples are in closer resemblance to the dimples on the notched tension specimens than with those observed on the smooth specimens.

Partial flipping to other shear bands was observed at the macroscopic scale from the CT scans. SEM investigations could not reveal any obvious abnormalities on the fracture surfaces to explain the flipping. There is a possibility that strain localizes in these shear bands due to local heterogeneities, for instance in the particle distribution or in the local grain orientations, causing these occurrences. It is hard to investigate these local heterogeneities experimentally, but numerical investigations by, e.g., Tekoğlu and Nielsen (2019), support

the hypothesis. However, a detailed study of this phenomenon is outside the scope of the present paper.

5 Discussion

As for the failure strain in the notched tensile tests, the UIE and the UPE of the Kahn tear tests had a stronger reduction from the increased content of constituent particles than what was observed for the failure strain in the smooth tensile tests. Interestingly, the trends between the alloys for the UIE and the UPE did not correspond entirely with the trends observed for the tensile ductility. For 6061 the increased constituent-particle content had a stronger effect on the tensile ductility than for the other alloys. This was attributed to a shift towards larger particles from the A-alloy to the B-alloy, while for the other two alloys the particle size distribution was similar (for 6063) or shifted towards smaller particle sizes (for 6110). However, for the UIE and the UPE, the reduction from the A-alloy to the B-alloy was equal for 6061 and 6110, while 6063 had a smaller reduction. Thus, the differences in the reduction of the tear resistance cannot be solely attributed to differences in the particle size or be linked directly to the trends in tensile ductility. Bron et al. (2004) emphasized the importance of particle spacing on the tear resistance. The particle spacing was not monitored specifically in the current study, but a shift towards smaller particle sizes would imply an even higher number density/lower spacing and could thus be a factor affecting the reduction in tear resistance of 6110B. The presence of dispersoids in 6110 could possibly amplify the effect from the lower constituent-particle spacing in 6110B and hence contribute to the effect from the reduced spacing being stronger for 6110 than for the other two alloys. The lower effect on both the tensile ductility and the tear resistance for 6063 than for the other alloys could also be connected with the stronger tendency for intergranular fracture in 6063A than in 6063B, as indicated by the facets found on the fracture surface of the former alloy.

The differences in ductility further proved in the intensity of the strain fields and the localized necking measured on the CT scans. Still, there were no visible differences in the CT scans with respect to the fracture mode, neither between the A- and B-versions, nor between the alloys. Thus, the constituent particle content does not appear to influence the preferred fracture mode, and parameters the alloys have in common are attributed major influence on the fracture mode, particularly the low strain hardening, which is commonly emphasized in the literature as the main parameter [see, e.g., Hickey and Ravi-Chandar (2016)].

With DIC, lower strains were computed in the initial stage of the crack propagation, possibly related to the flat-to-slant transition. This could not be recognized in the CT scans as less necking. The DIC strain fields further showed strained bands angled between the crack propagation direction and the loading direction. These bands were also recognized in the CT scans as out-of-plane deformations, and were observed to often occur when there was a small, partial flip or any other unevenness at or close to the crack edge. This unevenness reduces the amount of material on that side of the specimen, and consequently facilitates deformation. The fact that the bands are slanted could possibly be related to tunnelling of the crack. The extension of an unevenness in the crack propagation direction towards the centre was visible on the fracture surface both in the CT scan renders and by SEM imaging of the specimen shown in Fig. 10, which had particularly intense strained bands and could possibly represent an extreme case. For most other cases, we were not able to distinguish such a clear extension of the crack edge roughness on the fracture surface.

Despite low resolution of the CT scans, and thus inability to carefully examine ongoing fracture mechanisms and features of the crack tip, there were indications on a certain tunnelling of the crack. In the present study, the main aim has been to compare the materials at a more overall level and, if possible, observe differences at various stages of the crack growth, while not capturing the finest details of the crack tip. A high-resolution scan would come at a cost of the field of view, and comparing the full cracks would not be feasible.

There were varying amounts of scatter in the measured force–NOD curves (see Fig. 4), a trend apparently coinciding with the trends in ductility/tear resistance. The test series with the least ductile alloy, 6110B, had one test with a peak force approximately 15% higher than the peak force of most of the other tests in the series. The fracture surface of the specific specimen was studied in the SEM and compared to another specimen in the test series to search for possible explanations for the high peak, such as notably less constituent particles, but nothing particular was found. That precise specimen was notably thicker than the other specimens in

the series, but not enough to account for the difference in the force, and not enough to be affecting the peak force substantially.

6 Concluding remarks

In this study, the tear resistance of three 6000-series aluminium alloys in temper T6 was studied. For each alloy, there were one commercial version (A-alloy) and one version with increased content of constituent particles (B-alloy), where the B-alloy had a constituent-particle content of approximately three times that of the A-alloy. The aim was to study the effect of this increased constituent-particle content on the tear resistance, but also to investigate if there were any effects on the fracture mode or the fracture mechanisms. The study is a continuation of the studies by Thomesen et al. (2020) and Tomstad et al. (2021), where the tensile ductility of the alloys was investigated experimentally.

The unit initiation and unit propagation energies, characterizing the tear resistance of the alloys, were notably lower for the B-alloys compared to the A-alloys. The UIE was reduced by approximately 40% for alloy 6063, and by approximately 60% for alloys 6061 and 6110. The UPE was approximately halved for alloy 6063 and reduced by two thirds for 6061 and 6110. As for the failure strain in the notched tensile tests, the tear resistance in the Kahn tear tests was more strongly affected by a higher content of constituent particles than the failure strain in the smooth tensile tests was. Alloy 6063 was less affected by the increased content of constituent particles than the other alloys both in terms of tensile ductility and tear resistance. While the tensile ductility of alloy 6110 was less affected by the increase in constituent-particle content than the tensile ductility of 6061, the tear resistance was affected equally for the two alloys. The overall fracture mode was the same for the A- and B-alloys with a slant fracture after a flat-to-slant transition. There were no apparent major differences in the fracture mechanisms, but the B-alloys had somewhat smaller dimples than the A-alloys, in accordance with the lower ductility and tear resistance. The slant crack had a more coarse fracture surface in the centre than towards the edges of the crack, displaying a tensile-dominated fracture mechanism in the centre and a more shear-dominated fracture mechanism towards the edges.

Acknowledgements The authors gratefully appreciate the financial support from the Norwegian University of Science and Technology (NTNU) and the Research Council of Norway through the FRINATEK Programme FractAl, Project No. 250553, and through the Centre for Advanced Structural Analysis (CASA), Project No. 237885. The authors would like to thank Asle Joachim Tomstad for providing force–diameter data from the tensile tests and constituent particle counts on the B-alloys and Trond Auestad for managing the experiments. Laboratory responsible engineer Ole Tore Buset at the X-ray laboratory at NTNU is gratefully acknowledged for performing and reconstructing the CT scans.

Author contributions KQ: All except SEM study: Formal analysis, Investigation, Writing—original draft, Writing—review & editing, Visualization. ST: SEM study and Materials and experimental background: Formal analysis, Investigation, Writing—original draft, Writing—review & editing, Visualization. OSH: Conceptualization, Writing—review & editing, Supervision, Funding acquisition. TB: Conceptualization, Writing—review & editing, Supervision, Funding acquisition.

Funding Information Open access funding provided by NTNU Norwegian University of Science and Technology (incl St. Olavs Hospital - Trondheim University Hospital)

Conflict of interest The authors declare that they have no conflict of interest.

References

Ahrens J, Geveci B, Law C (2005) ParaView: an end-user tool for large-data visualization. In: Hansen CD, Johnson CR (eds) Chapter 36—the visualization handbook. Elsevier, Amsterdam, pp 717–731

ASTM Standard B871–01 (2001) Standard test method for tear testing of aluminum alloy products. ASTM International, West Conshohocken, PA

Blind JA, Martin JW (1983) The effect of dispersoids on the ductile fracture toughness of Al–Mg–Si alloys. Mater Sci Eng 57(1):49–54. https://doi.org/10.1016/0025-5416(83)90026-5

Broek D (1973) The role of inclusions in ductile fracture and fracture toughness. Eng Fract Mech 5(1):55–66. https://doi.org/10.1016/0013-7944(73)90007-6

Bron F, Besson J, Pineau A (2004) Ductile rupture in thin sheets of two grades of 2024 aluminum alloy. Mater Sci Eng A 380(1):356–364. https://doi.org/10.1016/j.msea.2004.04.008

Buljac A, Taillandier-Thomas T, Morgeneyer TF, Helfen L, Roux S, Hild F (2016) Slant strained band development during flat to slant crack transition in AA 2198 T8 sheet: in situ 3D measurements. Int J Fract 200(1–2):49–62. https://doi.org/10.1007/s10704-015-0052-z

Buljac A, Hild F, Helfen L, Morgeneyer TF (2018) On deformation and damage micromechanisms in strong work hardening 2198 T3 aluminium alloy. Acta Mater 149:29–45. https://doi.org/10.1016/j.actamat.2018.01.026

Çelik Ş, Andersen RG, Tekoğlu C, Nielsen KL (2021) On the dependence of crack surface morphology and energy dissipation on microstructure in ductile plate tearing. Int J Fract 230(1–2):115–132. https://doi.org/10.1007/s10704-020-00513-8

Dumont D, Deschamps A, Bréchet Y (2003) On the relationship between microstructure, strength and toughness in AA7050 aluminum alloy. Mater Sci Eng A 356(1–2):326–336. https://doi.org/10.1016/S0921-5093(03)00145-X

El-Naaman SA, Nielsen KL (2013) Observations on Mode I ductile tearing in sheet metals. Eur J Mech A 42:54–62. https://doi.org/10.1016/j.euromechsol.2013.04.007

Fagerholt E (2017) eCorr v4.0 Documentation. http://folk.ntnu.no/egilf/ecorr/doc/. Accessed 10 Dec 2019

Frodal BH, Christiansen E, Myhr OR, Hopperstad OS (2020) The role of quench rate on the plastic flow and fracture of three aluminium alloys with different grain structure and texture. Int J Eng Sci 150:103257. https://doi.org/10.1016/j.ijengsci.2020.103257

Ghahremaninezhad A, Ravi-Chandar K (2012) Ductile failure behavior of polycrystalline Al 6061–T6. Int J Fract 174(2):177–202. https://doi.org/10.1007/s10704-012-9689-z

Hahn GT, Rosenfield AR (1975) Metallurgical factors affecting fracture toughness of aluminum alloys. Metall Trans A 6(4):653–668. https://doi.org/10.1007/BF02672285

Hickey WF, Ravi-Chandar K (2016) Transition from flat to slant fracture in ductile materials. In: Hütter G, Zybell L (eds) Chapter 9—recent trends in fracture and damage mechanics, 1st edn. Springer International Publishing, Cham, pp 215–235. https://doi.org/10.1007/978-3-319-21467-2

James MA, Newman JC Jr (2003) The effect of crack tunneling on crack growth: experiments and CTOA analyses. Eng Fract Mech 70(3–4):457–468. https://doi.org/10.1016/S0013-7944(02)00131-5

Liu G, Zhang GJ, Ding XD, Sun J, Chen KH (2004) The influences of multiscale-sized second-phase particles on ductility of aged aluminum alloys. Metall Mater Trans A 35A(6):1725–1734. https://doi.org/10.1007/s11661-004-0081-0

Morgeneyer TF, Proudhon H, Besson J (2010) Study of the flat to slant crack transition in ductile thin sheet material: simulations and experiments. In: Fracture of materials and structures from micro to macro scale—ECF 18, Dresden, p 8. https://hal-mines-paristech.archives-ouvertes.fr/hal-00541090

Morgeneyer TF, Taillandier-Thomas T, Helfen L, Baumbach T, Sinclair I, Roux S, Hild F (2014) In situ 3-D observation of early strain localization during failure of thin Al alloy (2198) sheet. Acta Mater 69:78–91. https://doi.org/10.1016/j.actamat.2014.01.033

Myhr OR, Grong Ø, Schäfer C (2015) An extended age-hardening model for Al–Mg–Si alloys incorporating the room-temperature storage and cold deformation process stages. Metall Mater Trans A 46(12):6018–6039. https://doi.org/10.1007/s11661-015-3175-y

Nielsen KL, Gundlach C (2017) Crack tip flipping under mode I tearing: investigated by X-ray tomography. Int J Solids Struct 118–119:119–127. https://doi.org/10.1016/j.ijsolstr.2017.04.014

Pardoen T, Hachez F, Marchioni B, Blyth PH, Atkins AG (2004) Mode I fracture of sheet metal. J Mech Phys Solids 52(2):423–452. https://doi.org/10.1016/S0022-5096(03)00087-5

Petit T, Besson J, Ritter C, Colas K, Helfen L, Morgeneyer TF (2019) Effect of hardening on toughness captured by stress-based damage nucleation in 6061 aluminum alloy. Acta Mater 180:349–365. https://doi.org/10.1016/j.actamat.2019.08.055

Polmear IJ (2006) Light alloys: from traditional alloys to nanocrystals, 4th edn. Butterworth-Heinemann, Oxford

Rasband WS (1997–2018) ImageJ. U.S. National Institutes of Health, Bethesda. https://imagej.nih.gov/ij/

Shen Y, Morgeneyer TF, Garnier J, Allais L, Helfen L, Crépin J (2013) Three-dimensional quantitative in situ study of crack initiation and propagation in AA6061 aluminum alloy sheets via synchrotron laminography and finite-element simulations. Acta Mater 61(7):2571–2582. https://doi.org/10.1016/j.actamat.2013.01.035

Srivastava A, Ponson L, Osovski S, Bouchaud E, Tvergaard V, Needleman A (2014) Effect of inclusion density on ductile fracture toughness and roughness. J Mech Phys Solids 63(1):62–79. https://doi.org/10.1016/j.jmps.2013.10.003

Sutton MA, Zhao W, Boone ML, Reynolds AP, Dawicke DS (1997) Prediction of crack growth direction for mode I/II loading using small-scale yielding and void initiation/growth concepts. Int J Fract 83(3):275–290. https://doi.org/10.1023/A:1007339625267

Tekoğlu C, Nielsen KL (2019) Effect of damage-related microstructural parameters on plate tearing at steady state. Eur J Mech A 77:103818. https://doi.org/10.1016/j.euromechsol.2019.103818

Thomesen S (2019) Plastic flow and fracture of isotropic and anisotropic 6000-series aluminium alloys: experiments and numerical simulations. PhD Thesis, Norwegian University of Science and Technology, Trondheim

Thomesen S, Hopperstad OS, Myhr OR, Børvik T (2020) Influence of stress state on plastic flow and ductile fracture of three 6000-series aluminium alloys. Mater Sci Eng A 783:139295. https://doi.org/10.1016/j.msea.2020.139295

Tomstad AJ, Thomesen S, Børvik T, Hopperstad OS (2021) Effects of constituent particle content on ductile fracture in isotropic and anisotropic 6000-series aluminium alloys. Mater Sci Eng A 820:141420. https://doi.org/10.1016/j.msea.2021.141420

Westermann I, Pedersen KO, Furu T, Børvik T, Hopperstad OS (2014) Effects of particles and solutes on strength, work-hardening and ductile fracture of aluminium alloys. Mech Mater 79:58–72. https://doi.org/10.1016/j.mechmat.2014.08.006